INORGANIC CHEMISTRY FRONTIERS

CCS 中国化学会 CHINESE CHEMICAL SOCIETY

ROYAL SOCIETY OF CHEMISTRY

Ternary Ag-TiO2/Reduced Graphene Oxide Nanocomposite as Anode Material for Lithium Ion Battery

Journal:	*Inorganic Chemistry Frontiers*
Manuscript ID	QI-RES-05-2019-000576.R1
Article Type:	Research Article
Date Submitted by the Author:	28-Jun-2019
Complete List of Authors:	Yu, Jiuling; New Mexico State University Huang, Di; New Mexico State University, Chemical Engineering Liu, Yanan ; Beijing University of Chemical Technology Luo, Hongmei; New Mexico State University,

Ternary Ag-TiO_2/Reduced Graphene Oxide Nanocomposite as Anode Material for Lithium Ion Battery

Jiuling Yu,[a] Di Huang,[a] Yanan Liu,[b] Hongmei Luo[a,*]

[a]Department of Chemical and Materials Engineering, New Mexico State University, Las Cruces, NM 88003, USA.

[b]State Key Laboratory of Chemical Resource Engineering, Beijing University of Chemical Technology, 100029, China.

* Corresponding author. E-mail: hluo@nmsu.edu

Abstract

Developing high-performance anode materials for rechargeable lithium-ion batteries (LIBs) is of great importance for large-scale applications of electronics and electric vehicles. Here, silver-doped titanium dioxide nanoparticles on the reduced graphene oxide sheets (denoted as Ag-TiO_2/rGO) nanocomposite is synthesized through a solvothermal method. With the merits of high surface area of rGO and high conductivity of Ag nanoparticles, Ag-TiO_2/rGO shows the competitive reversible capacity of 196.9 mA h g^{-1} at a current density of 1 C after 100 cycles. In the meanwhile, the high rate capability and cyclability can be maintained. After a long-term cycling of 1000 cycles at 5 C, the discharge capacity is still as high as 144.2 mAh g^{-1} with nearly 100% Coulombic efficiency. Therefore, Ag-TiO_2/rGO, as a potential anode material, exhibits a superior stable property for the long-life LIBs, and also builds up a pathway for further studies on fabrication of ternary nanomaterials in electrochemical energy storage applications.

Introduction

Nowadays, with the excessive depletion of fossil fuels, environmental problems have undisputedly become one of the most concerns to the society. Thus, it is extremely urgent to explore variety of green energy resources to relieve environmental problems. Rechargeable lithium-ion batteries (LIBs) are highly demanded as promising candidate of electrochemical energy storage devices.[1, 2] Additionally, the growing requirements for high-performance LIBs promotes the development of the new-generation LIBs with high density of energy and power, long-term life span and stable capacity. Recently, versatile electrode materials have been investigated to achieve the superior performances, especially the transition metal oxides as anode materials by virtue of more Li incorporation capability and nanostructures.[3-8] Among the transition metal oxides, titanium dioxide (TiO_2), is chosen as a potential anode material owing to its low volume expansion (~4%) during Li^+ insertion/ extraction reaction, high rate capability, low cost and eco-friendliness.[9-11] Four polymorphs of TiO_2 (anatase, rutile, brookite and TiO_2-B) are commonly investigated as anode materials, especially anatase TiO_2. Nevertheless, anatase TiO_2 with space group $I4_1/amd$ merely uptakes 0.5 Li^+ per Ti atom during Li^+ insertion, resulting in its theoretical specific capacity of 168 mAh g^{-1}.[12] Therefore, the development of high-performance TiO_2-based LIBs is greatly hindered by its low theoretical specific capacity and poor ionic and electrical conductivity (~10^{-12} S m^{-1}). It remains challenging to improve the capacity of TiO_2-based material as anode of LIBs with maintaining its merits.

Up to date, there are three main strategies to enhance the kinetics and electrical conductivity of TiO_2 in the lithium storage. The first strategy is to synthesize nanostructured material with diverse morphologies. As the size of bulk material is decreased at nano-grade, the connection

of electrode and electrolyte will significantly increase, and the pathway of Li^+ diffusion will be shortened, so as to improve the kinetics of electrode.[13, 14] Lee *et al.* reported the fabrication of hollow TiO_2 nanostructure consisting of 5 nm nanocrystals with superior lithium storage capability and stable ability.[11] Nevertheless, agglomeration of nanoparticles during fast repeated Li^+ insertion/extraction is still a barrier. The second strategy is to introduce carbon-based materials as conductive media, for example, carbon[15, 16], carbon nanofibers,[17] carbon nanotubes,[18] and reduced graphene oxide,[9] using hydrothermal/solvothermal,[9, 15] electrospinning,[17] atomic layer deposition,[18] microwave-assisted forced-hydrolysis,[19] and sol-gel methods.[20] Particularly, reduced graphene oxide (rGO), a two-dimension (2D) material with high surface area and high conductivity, can be used to increase the electron and ion transfer rate. In addition, TiO_2 nanoparticles tend to disperse uniformly on the rGO sheet, which can alleviate its agglomeration during cycling. Anchoring TiO_2 nanoparticles can also inhibit rGO sheet restacking. The third strategy is combining TiO_2 with other metal or metal oxide to achieve high capacity. Madian *et al.* demonstrated that the synthesis of TiO_2/CoO nanotubes with significantly enhanced electrochemical performance.[21] Also, Wang *et al*. proposed hybrid TiO_2-MoO_3 core–shell nanowire array, which exhibited higher gravimetric capacity and better cyclability.[22] Silver (Ag), a noble metal with high electronic conductivity, is a promising candidate of anode material as well. Luo *et al*. reported nanofibrous silver-nanoparticle/anatase–rutile-titania composite exhibited higher charge/discharge performances than commercial P25.[23]

Considering the above approaches, ternary nanocomposite composed of metal/metal oxide/ carbon-based material may offer new opportunities to be anode material in LIBs. Thus, the

ternary nanocomposite of Ag doped TiO_2 on the rGO surface is expected to improve Li storage properties owing to fast electron transfer pathway and high conductivity. In this work, Ag-TiO_2/rGO nanocomposite is fabricated via a solvothermal method. The effect of rGO layer is not only to avoid agglomeration of TiO_2 nanoparticle, but also to be a conductive substrate with high specific surface area. The nanosized Ag particles contribute to enhanced electrochemical performance by increasing intra- or inter-grain connectivity.

Experimental

Chemicals

All chemicals were used without further purification. Graphite flakes (>99.9%) was purchased from MTI Corporation. Sodium nitrate ($NaNO_3$, ≥99.0%), sulfuric acid (H_2SO_4, 95-98.0%), potassium permanganate ($KMnO_4$, ≥99.0%), hydrogen peroxide solution (H_2O_2, 30% (w/w) in H_2O), silver acetate (CH_3COOAg, ≥99.0%), sodium dodecyl sulfate (SDS, ≥98.5%), titanium(IV) isopropoxide (TTIP, 97%) and anhydrous ethyl alcohol (C_2H_5OH) were supplied by Sigma-Aldrich. Hydrochloric acid (HCl, 37.6%) and potassium chloride (KCl, ≥99.0%) were bought from Fisher Scientific.

Materials synthesis

The synthesis procedure for Ag-TiO_2/rGO nanocomposite is shown in Scheme 1.

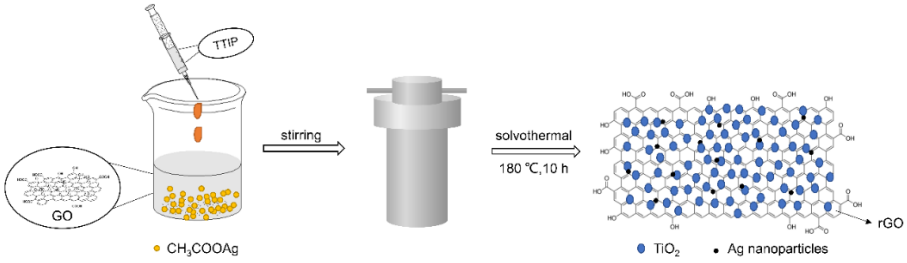

Scheme 1. Schematic diagram of the synthetic steps for Ag-TiO_2/rGO nanocomposite.

Graphene oxide (GO) was synthesized via a modified Hummer's method.[24,25] Briefly, a mixture of 4 g graphite flakes and 2 g $NaNO_3$ in 100 ml concentrated H_2SO_4 was kept in the ice bath with continuous stirring. 20 g $KMnO_4$ was added into above solution and stirred for 10 h. Then, 300 ml DI water and 3 ml H_2O_2 solution were gradually added and stirred for another 2 h under the ice bath condition. Subsequently, the obtained solution was filtered and washed by DI water, 37% HCl and ethanol for 3 times. At last, the product was dried in a vacuum oven overnight.

To prepare Ag-TiO_2/rGO, 20 mg collected graphene oxide sheet was re-dispersed in the DI water and stirred for 2 h to form uniform GO solution. Next, 8.5 mg CH_3COOAg was dissolved in 5 ml DI water and its solution was dropwise added into GO solution under magnetic stirring for 12 h. Subsequently, the mixture of 10 mg SDS and 5 mg KCl in 5 ml DI water was added into the above solution and kept stirring for 0.5 h. 10 ml absolute ethanol with 0.5 ml TTIP was followed to add into the solution slowly. After another 0.5 h continuous stirring, the final solution was transferred into a 50 ml Teflon-lined autoclave and maintained at 180 ℃ for 10 h. The black composite was finally centrifuged and rinsed with DI water, then dried at 45 ℃ in the vacuum oven overnight. This final product was named as Ag-TiO_2/rGO. As compared samples, TiO_2/rGO was prepared without adding CH_3COOAg, and TiO_2 prepared without adding CH_3COOAg and GO sheet. Moreover, to investigate the effect of each component on the morphology, Ag-TiO_2/5_rGO was synthesized using 5 mg graphene oxide, while Ag-1_TiO_2/rGO was prepared by adding 1 ml TTIP. All samples were synthesized under the same condition. To prove the synergistic effect, 2.2 wt% Ag and 97.8 wt% solvothermal-synthesized TiO_2/rGO was mechanically mixed together and named as M_Ag-TiO_2/rGO. The other compared sample for synergistic reaction was prepared by mechanically mixed 2.2 wt% Ag,

88.1 wt% solvothermal-synthesized TiO_2 and 9.7 wt% rGO, named as M_Ag-TiO_2-rGO. Ag was directly obtained by annealing CH_3COOAg at 350 ℃ for 1h.

Characterization

X-ray diffraction (XRD) was used to determine the samples' phase and structure, obtained from PANalytical Empyrean X-Ray diffractometer using Cu Kα (λ=1.5406 Å) at 45 kV/40 mA in the 2θ range of 10-80°. The weight percent of rGO in the sample was examined by thermogravimetric analysis (TGA) on Q500, TA instruments from 20 ℃ to 800 ℃ at the heating rate of 10 ℃/min and air flow rate of 60 ml/min. A PerkinElmer Elan DRC-E inductively coupled plasma mass spectrometer (ICP-MS) was employed to measure the metal loading in the sample. Fourier-transform infrared spectroscopy (FT-IR) using a Spectrum Two FT-IR spectrophotometer by PerkinElmer was applied for characterizing the chemical functional groups. Nitrogen adsorption/desorption isotherms and pore size distributions were conducted on a Micromeritics Micromeritics ASAP 2050 High Pressure Sorption Analyzer at 77 K. The morphology and particle size were characterized by transmission electron microscopy (TEM) via H-7650 from Hitachi High-Technologies Corporation, high-resolution transmission electron microscope (HRTEM) via JEOL JEM-2100F and S-3400N Type II scanning electron microscopy (SEM) by Hitachi High-Technologies Corporation. Elemental distribution was analyzed by energy dispersive X-ray spectroscopy (EDX).

Electrochemical experiment

The electrochemical experiments were carried out using CR2025 coin cells with as-obtained working electrode, separator, and lithium chip in an argon-filled glove-box. The moisture and oxygen contents in the glove-box were maintained below 1 ppm. To prepare the working

electrode, the electrode slurry was firstly prepared by mixing active materials, carbon black and carboxymethyl cellulose (CMC) in DI water at a weight ratio of 8:1:1. The mass loading of the working electrodes is in the range of 1.0-1.5 mg. And then, the slurry was casted on the copper foil and dried in the vacuum oven. The electrolyte was a mixture of 1 M $LiPF_6$ in ethylene carbonate/dimethyl carbonate with volume ratio of 1:1. The galvanostatic charge and discharge performances were measured using a NEWARE battery testing instrument under various current densities (1 C = 168 mA g^{-1}) with a voltage range of 0.1-3.0 V vs. Li/Li^+ at room temperature. A CHI electrochemical instrument was used to collect cyclic voltammetry (CV) curves in the range of 0.001-3 V vs. Li/Li^+ at a scan rate of 0.1 mV s^{-1} and electrochemical impedance spectroscopy (EIS) measurements in the range from 100 kHz to 0.01 Hz by applying a 5 mV amplitude.

Results and discussion

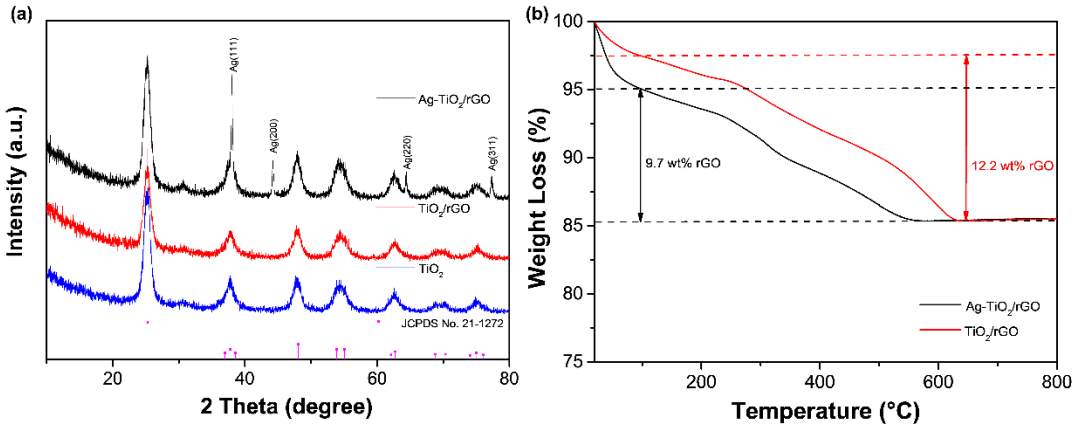

Figure 1. (a) XRD patterns of Ag-TiO_2/rGO, TiO_2/rGO and TiO_2; and (b) TGA curves of Ag-TiO_2/rGO and TiO_2/rGO.

The crystallization of synthesized samples is revealed through XRD, as displayed in Figure 1(a) and S1. The main peaks at 25.4°, 37.7°, 47.8°, 55.0°, 62.5°, 68.9° and 75.1° in Figure 1(a) are identified to the reflections of (101), (004), (200), (211), (204), (116) and (215), which is

the proof of TiO_2 formation in anatase phase (JCPDS No. 21-1272). The wide peak and low intensity indicate the small grain size of synthesized TiO_2. According to Scherrer equation, the grain size is evaluated to be ~10 nm, which is further confirmed in TEM image. As shown in Figure S1, a broad peak of GO at 11.3° is observed. However, the typical peak of GO disappears in Ag-TiO_2/rGO and TiO_2/rGO because GO has been reduced to rGO, whose typical peak is at around 24° and overlaps with the (101) peak in TiO_2.[26] In addition, four extra diffraction peaks at 38.1°, 44.2°, 64.4° and 77.4° exclusively appear in the sample of Ag-TiO_2/rGO. These peaks are indexed to the (111), (200), (220) and (311) planes of Ag (JCPDS No. 04-0783),[27] indicating the successful synthesis of ternary Ag-TiO_2/rGO nanocomposite.

The contents of rGO in Ag-TiO_2/rGO and TiO_2/rGO are determined by TGA, as shown in Figure 1(b). Before 100 °C, around 5% weight loss from Ag-TiO_2/rGO and 2.5% weight loss from TiO_2/rGO are mainly due to water evaporation. From 100 °C to 650 °C, 9.7 wt% in Ag-TiO_2/rGO and 12.2 wt% in TiO_2/rGO are contributed to the amount of rGO in the composite. Due to the introduction of Ag, the composition ratio of rGO in Ag-TiO_2/rGO is lower than that of TiO_2/rGO. There is no obvious mass change after heating up to 650 °C. The composition ratio of metal in the composite is evaluated by ICP-MS analysis. Concentration of Ag in the ternary nanocomposite is 2.2 wt%. Thus, the mass ratio of Ag to TiO_2 in Ag-TiO_2/rGO is 1: 38.8 and the typical yield from CH_3COOAg to Ag is 61.68%.

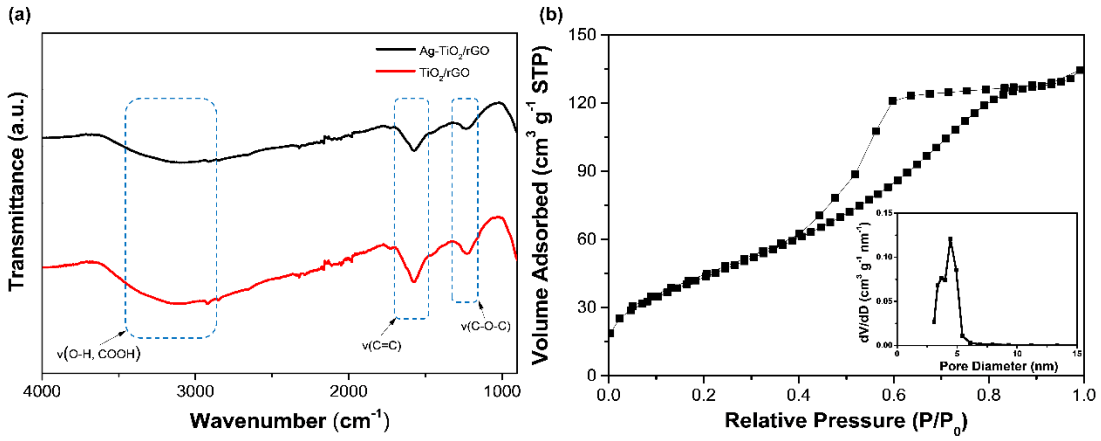

Figure 2. (a) FT-IR spectra of Ag-TiO_2/rGO and TiO_2/rGO; and (b) Nitrogen adsorption/desorption isotherms and pore size distribution (insert) of Ag-TiO_2/rGO.

Different functional groups of the composites are displayed in the spectrum of FT-IR, as seen in Figure 2(a). Three typical peaks at ~3200, 1580, 1225 cm^{-1} are observed in both Ag-TiO_2/rGO and TiO_2/rGO.[28] A broad peak from 2800 to 3400 cm^{-1} could be attributed to stretching vibrations of O-H (e.g. hydroxyl group in carboxylic acid). An evident peak at 1580 cm^{-1} is from C=C skeletal vibration. A weak peak at 1225 m^{-1} is due to the epoxy C-O-C stretching vibration.[28, 29] Such vibrations from oxygenated functional groups and C=C skeleton are indicative of the existence of rGO in the synthesized samples.

Surface area of synthesized samples is determined by N_2 adsorption-desorption isotherms. As displayed in Figures 2(b) and S2, all these isotherms show a distinct Type H2(b) hysteresis loop, which can be classified to Type IV isotherm.[30] It implies the existence of mesopores in the samples. The surface area is calculated via Brunauer-Emmett-Teller (BET) method, while pore volume and pore size are evaluated based on Barrett–Joyner–Halenda (BJH) desorption branch, as listed in Table S1. Compared with pure TiO_2 (149.20 m^2 g^{-1}), other two samples anchored on the rGO sheet have larger surface areas (160.50 m^2 g^{-1} of Ag-TiO_2/rGO and 168.75 m^2 g^{-1}

of TiO_2/rGO). However, there is no significant increase on the surface area, since the amount of rGO in the composite is limited. It must be mentioned that the surface area of Ag-TiO_2/rGO is smaller than that of TiO_2/rGO due to the relative lower content of rGO in Ag-TiO_2/rGO, which is confirmed by TGA results. The corresponding pore size distributions are shown in the insert figures of Figures 2(b) and S2, in which pore size of TiO_2 (5.18 nm) is slightly bigger than that of other samples (4.50 nm of Ag-TiO_2/rGO and 4.28 nm of TiO_2/rGO). It's probably because particles tend to form a more homogeneous dispersion after depositing on rGO surface.[14] Therefore, the enlarged surface area and mesopores will shorten the diffusion distance, which will contribute to faster transports of electrolyte and Li^+ in the discharge/charge process.[31]

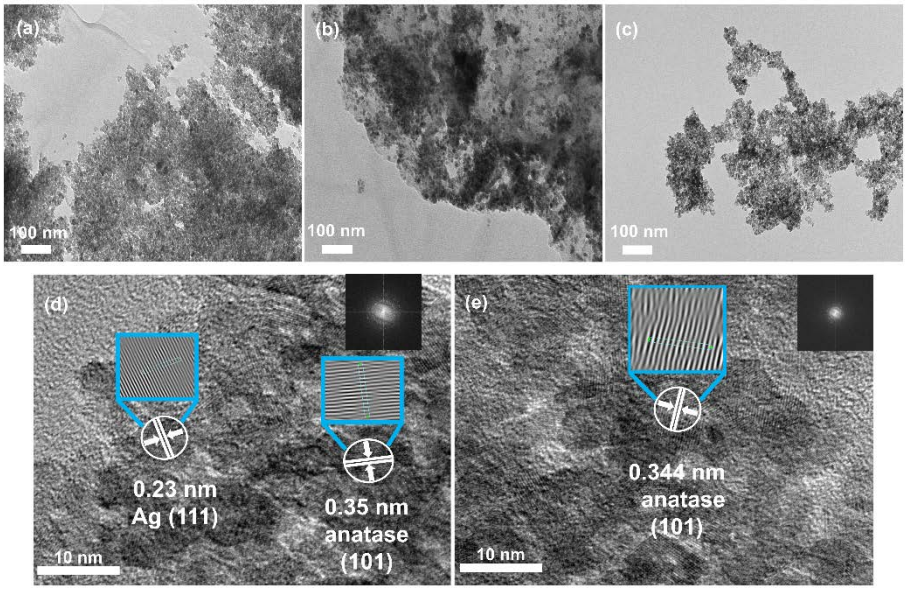

Figure 3. TEM images of (a) Ag-TiO_2/rGO; (b) TiO_2/rGO; and (c) TiO_2. HRTEM images and SAED patterns (inset) of (d) Ag-TiO_2/rGO; and (e) TiO_2/rGO.

The morphologies and microstructures of synthesized nanocomposites are investigated by TEM and SEM, as shown in Figures 3, S3 and S4. In Figure 3(a-c), TEM images of Ag-TiO_2/rGO, TiO_2/rGO, and TiO_2 are presented. The wrinkled rGO sheet can be clearly observed in Figure

3(a), and the ultra-small TiO_2 particles are distributed uniformly on the rGO surface. The thin 2D structure of rGO can provide an efficient transport channel for electrons during the insertion/extraction process.[14] Ag nanoparticles are rarely identified in Figure 3(a), since their lower content relative to TiO_2 in the sample. As shown in Figure 3(b), TiO_2 particles deposit dispersedly on rGO and almost cover the whole surface. While a flimsy layer is observed, which points to the formation of rGO. Pure TiO_2 is composed of numerous small nanoparticles with a similar morphology to the other two nanocomposites, shown in Figure 3(c). Yu *et al*.[32] reported that TiO_2 powder contains many aggregates after hydrothermal reaction. Here, the obtained TiO_2 shows a good distribution without severe aggregation, owing to the addition of surfactant SDS. Compared to pure TiO_2, TiO_2 aren't anchored so compactly on the rGO surface with rGO addition. The extra space between TiO_2 nanoparticles will provide more diffusion path, thereby contributing to the enhanced ion/charge transfer. Moreover, the role of rGO is to afford conductive matrix during the Li^+ insertion/extraction process.[26] It should be pointed out that, during the solvothermal process, the sizes of all three nanocomposites are extremely small (~10 nm), which is consistent with the XRD results.

HRTEM images of Ag-TiO_2/rGO and TiO_2/rGO are displayed in Figure 3(d) and (e), respectively. The inserts are magnifications of lattice fringes and selected-area electron diffraction (SAED) patterns. The interplanar spacing of 0.35 nm in Figure 3(d) is corresponding to the (101) plane of anatase TiO_2, while 0.23 nm reflects the (111) plane of Ag. Thus, it can be verified that Ag and TiO_2 nanoparticles are anchored on the surface of rGO. In addition, d-spacing of anatase (101) plane is calculated to be 0.344 nm in TiO_2/rGO, which is consistent with diffraction ring (101) of the SAED pattern. To evaluate the relationship between the

amount of each species and the morphology, samples with different ratios of rGO and TiO_2 are synthesized. In Figure S3(a, b), TEM images do not show a distinct difference on the morphology. However, for the compared samples (M_Ag-TiO_2/rGO and M_Ag-TiO_2-rGO), it is clearly to see that the TiO_2 particles tend to agglomeration and nonuniform distribution, as displayed in Figure S3(c, d). The structure and element distribution are further confirmed in SEM and EDX mappings in Figure S4. Spheres with diameter ~1 μm, which are aggregations of ultra-fine particles due to the high surface energy,[33] are dispersed on the rGO layer, as shown in Figure S4(a). EDX mappings in Figure S4(b, c) indicate Ag, Ti, O, and C elements distribute evenly on the sample surface, demonstrating a successful fabrication of Ag-TiO_2/rGO nanocomposite.

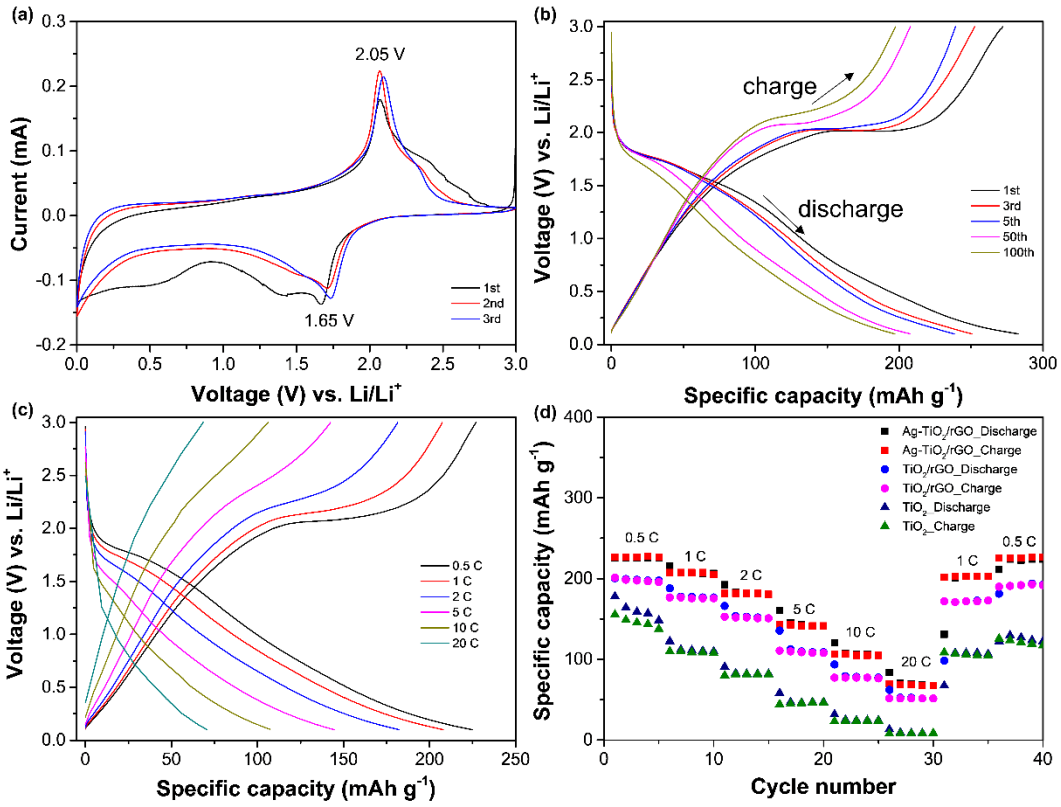

Figure 4. (a) Cyclic voltammetry curves of Ag-TiO_2/rGO at a scan rate of 0.1 mV s^{-1}; (b) Galvanostatic discharge/charge voltage profiles of Ag-TiO_2/rGO for the 1st, 3rd, 5th, 50th, 100th cycle at a current density of 1 C; (c) Discharge/charge voltage profiles of Ag-TiO_2/rGO

at virous current densities (0.5 C, 1 C, 2 C, 5 C, 10 C and 20 C); and (d) Rate capabilities of Ag-TiO_2/rGO, TiO_2/rGO and TiO_2 at various current densities from 0.5 C to 20 C.

The synergetic effect between Ag and TiO_2 nanoparticles on the ultra-thin graphene network endows the ternary Ag-TiO_2/rGO nanocomposite as a potential anode material in LIBs. Therefore, the electrochemical property is performed using CR2025 coin typed half cells. Firstly, to understand the reduction and oxidation processes on the electrodes, CV curves for the initial three cycles of Ag-TiO_2/rGO are plotted in Figure 4(a), under 0.001-3 V (vs. Li/Li^+) at a 0.1 mV s^{-1} scan rate. During the lithium intercalation process, a cathodic peak of 1.65 V is observed in the initial cycle, which represents the valence state change from Ti^{4+} to Ti^{3+}. An anodic peak is located at 2.05 V in the de-intercalation process from TiO_2. The redox peak of Ti^{4+}/Ti^{3+} of 2nd and 3rd cycles shift slightly to the high voltage due to irreversible reactions.[34] But a good cycling performance is also reflected in the CV based on the similar shapes of 2nd and 3rd cycles.[16] This whole electrochemical reaction is expressed as the following equation:[35]

$$TiO_2 + xLi^+ + xe^- \leftrightarrow \ Li_xTiO_2 \ \ (0 \le x \le 1) \qquad \text{Eq. (1)}$$

where x is the insertion ratio of Li. For anatase phase of TiO_2 with tetragonal structure, maximum insertion ratio is equal to 0.5.

As depicted in Figure 4b, galvanostatic discharge/charge voltage profiles of ternary Ag-TiO_2/rGO nanocomposite are shown in a voltage window of 0.1-3 V (vs. Li/Li^+) for the 1st, 3rd, 5th, 50th, 100th cycle at 1 C. The discharge and charge capacities of the first cycle are 283.0 mAh g^{-1} and 272.4 mAh g^{-1}, respectively. To compare the difference of electrochemical performance in the three synthesized samples, galvanostatic discharge/charge curves of the other two samples are evaluated and shown in Figure S5. Even though their initial discharge

capacities are both higher than that of Ag-TiO_2/rGO, their discharge capacities are declining rapidly in the third cycle. Additionally, their Coulombic efficiencies are lower than that of Ag-TiO_2/rGO (96.3%), which are 62.6% for TiO_2/rGO and 36.8% for TiO_2 in the first cycle. The irreversible capacity loss is mainly due to the formation of the solid electrolyte interface (SEI).[36-38] Notwithstanding, stable SEI also contributes to the following cycles with a high Coulombic efficiency. After three cycles, Coulombic efficiencies for all three samples are above 95%, suggesting the competitive reversible capacities during lithium insertion/extraction processes. Furthermore, after 100 discharge/charge processes, the discharge capacity of Ag-TiO_2/rGO still remains 196.9 mAh g^{-1}, accounting for 69.6% of the first discharge capacity, which is superior to that of TiO_2/rGO (172.7 mAh g^{-1}) with 45.5% retention and TiO_2 (91.4 mAh g^{-1}) with 23.8% retention. It can be concluded that addition of reduced graphene oxide acts as a conductive matrix to relieve the capacity fading during discharge/charge processes.[9] Simultaneously, introduction of Ag into TiO_2/rGO composite further enhances the electrochemical activity as the anode material. Two apparent plateaus at ~1.75 V (cathodic sweep) and 2.10 V (anodic sweep) are found in Figures 4(b) and S5, corresponding to lithium insertion to TiO_2 lattice and extraction from TiO_2 lattice, respectively, which is in accord with CV results.

Figure 4(c) shows the discharge/charge curves for Ag-TiO_2/rGO at different current densities. The specific capacity is decreased with the increasing current density. The discharge specific capacities are 225.2, 207.5, 182.8, 145.0, 120.3 and 70.8 mAh g^{-1} at 0.5, 1, 2, 5, 10 and 20 C, respectively. To compare the rate capabilities of three electrodes, their rate performances are displayed in Figure 4(d). It's obvious to observe that the specific capacities of all these

electrodes are well maintained as the current density is reduced back to 0.5 C, which implies their good rate capabilities during cycling. Notably, Ag-TiO_2/rGO exhibits the highest capacity, which is partially contributed by Ag addition.

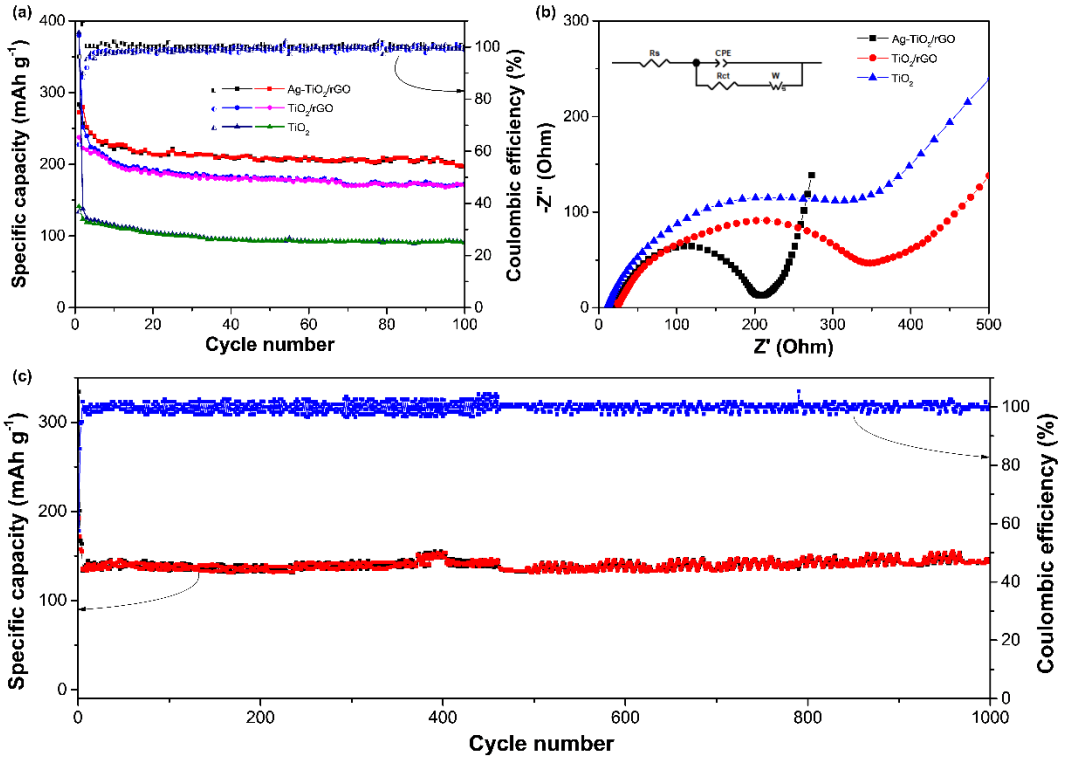

Figure 5. (a) Cycling performances of Ag-TiO_2/rGO, TiO_2/rGO and TiO_2 at a current density of 1 C and corresponding Coulombic efficiencies; (b) Nyquist plots of Ag-TiO_2/rGO, TiO_2/rGO and TiO_2 after 100 cycles; and (c) Cycling performance of Ag-TiO_2/rGO at 5 C for 1000 cycles and corresponding Coulombic efficiency.

The comparative cycling performances of Ag-TiO_2/rGO, TiO_2/rGO and TiO_2, and the relevant Coulombic efficiencies are given in Figure 5(a). Among three electrodes, Ag-TiO_2/rGO reveals the best stability with highest capacity, in agreement with the rate capability in Figure 4(d). Their better stabilities may be attributed to the low volume change of TiO_2 in the discharge/charge process. The enhanced capability of TiO_2/rGO, compared to bare TiO_2, is caused by the good electrical conductivity of rGO. In addition, Ag nanoparticles further improves the conductivity, and the Coulombic efficiency is retained at nearly 100% during 100

cycles. All results indicate that Ag-TiO_2/rGO has a great potential as anodes in LIBs. To identify the synergetic effect between Ag and TiO_2 on the graphene sheets, the cycling performance of M_Ag-TiO_2/rGO and M_Ag-TiO_2-rGO, prepared by a simple mechanical mixed method according to the composition ratio of each component, are examined and shown in Figure S6. It's clear to observe that after 50 cycles M_Ag-TiO_2-rGO shows an improved capacity (125.0 mAh g^{-1}) than bare TiO_2 (93.4 mAh g^{-1}). Although introducing both Ag and rGO, the capacity of M_Ag-TiO_2-rGO is even lower than that of TiO_2/rGO. The inferior cycling performance can be ascribed to the aggregation of Ag and TiO_2 on the rGO layer by mechanical mixing, verified in the Figure S3(c, d). In addition, mechanical mixture M_Ag-TiO_2/rGO, shown in Figure S6 displays a similar performance as TiO_2/rGO, indicating that mixing Ag with TiO_2/rGO by mechanical method could not contribute to improve the electrochemical performance. Therefore, we can conclude that the best cycling performance of Ag-TiO_2/rGO is the result of synergetic effect in Ag and TiO_2 nanoparticles on the rGO surface via solvothermal process. A comparison with other TiO_2-based anode materials is summarized in Table 1. The results show Ag-TiO_2/rGO nanocomposite has a competitive electrochemical performance than other reported materials up to now.

The EIS measurements are performed to investigate the kinetics reaction on the electrodes. Nyquist plots of Ag-TiO_2/rGO, TiO_2/rGO and TiO_2 after 100 cycles in the frequency range from 100 kHz to 0.01 Hz are presented in Figure 5(b). Each Nyquist plot consists of a compressed semicircle in the high frequency region and an oblique line in the low frequency region, unveiling the charge transfer process and Warburg diffusion process, respectively. The Randles equivalent circuit is modeled and shown in the insert of Figure 5(b), in which R_s

represents the electrolyte resistance, CPE is the constant phase element, R_{ct} means the charge transfer resistance, and W is the Warburg impedance.[39] Among the three electrodes, the diameter of semicircle from Ag-TiO_2/rGO is the smallest, indicating that the charge transfer resistance of Ag-TiO_2/rGO is lowest. According to equivalent circuit, the charge transfer resistances of Ag-TiO_2/rGO, TiO_2/rGO and TiO_2 are simulated to 187.4 Ω, 330.4 Ω and 395.3 Ω, respectively. The electronical conductivities (σ) can be obtained from the following equation:[40]

$$\sigma = \frac{L}{A \times R} \qquad \text{Eq. (2)}$$

where L is thickness, A is area, R is the fitted resistance of electrode pellets. The electronical conductivity for Ag-TiO_2/rGO (1.36×10^{-4} S cm^{-1}) is higher than those of TiO_2/rGO (7.71×10^{-5} S cm^{-1}) and TiO_2 (6.44×10^{-5} S cm^{-1}), which proves that the electronic conductivity can be increased with introduction of Ag and rGO.

This fact further confirms that the ternary Ag-TiO_2/rGO nanocomposite increases the charge transfer and conduces to better lithium storage property. An ultra-long cycling performance of Ag-TiO_2/rGO is observed at a high current density of 5 C, as shown in Figure 5(c). The discharge capacity can still be kept at 144.2 mA h g^{-1} after 1000 cycles with almost 100% Coulombic efficiency, which manifests Ag-TiO_2/rGO as a promising candidate anode material with a superior stability in a long-term process.

Table 1. Comparison of electrochemical performance for Ag-TiO_2/rGO nanocomposite and other reported TiO_2-based materials as anodes in LIBs.

Active material	**Current density**	**Capacity (mA h g^{-1})**	**Voltage condition (V)**	**Reference**
TiO_2 nanocrystal/RGO sheet	0.1 A g^{-1}	175 (100th)	1-3	[20]
Anisotropic TiO_2/graphene sandwich papers	0.168 A g^{-1}	180	1-3	[41]
TiO_2 quantum dots/graphene nanosheets	0.335 A g^{-1}	190 (100th)	1-2.5	[42]
Nitrogen-doped carbon foams-TiO_2-400	0.1 A g^{-1}	203	1-3	[43]
N-doped carbon-coated hollow urchin-like anatase TiO_2 spheres	0.1675 A g^{-1}	165.1 (200th)	1-3	[15]
Nitrogen-doped reduced graphene oxide and nanotubular TiO_2	1 C	150 (50th)	1-3	[44]
Ag/TiO_2 nanotubes	0.6 C	~100 (50th)	0.1-3	[45]
Nanofibrous silver-nanoparticle/anatase-rutile-titania composite	0.17 A g^{-1}	120 (100th)	1-3	[23]
TiO_2/Ag hollow fibers	1 C	130	1-3	[46]
Au@TiO_2 nanotube arrays (120 nm Au nanofilm)	100 μA cm^{-2}	185 (200th)	1-2.8	[47]
Ag-TiO_2/rGO	0.168 A g^{-1}	196.9 (100th)	0.1-3	This work

Conclusion

In summary, the ternary Ag-TiO_2/rGO nanocomposite is prepared by a solvothermal technique. Owing to uniform deposition of ultrafine Ag-TiO_2 nanoparticles on the rGO layer, the agglomeration of nanoparticles and restacking of rGO sheets are prevented. To evaluate as an

anode material for LIBs, Ag-TiO_2/rGO exhibits good reversible capacity (196.9 mAh g^{-1} after 100 cycles at 1 C) and cyclability (144.2 mAh g^{-1} after 1000 cycles at 5 C) with almost 100% Coulombic efficiency. The superior electrochemical performance can be contributed to the synergetic effect between Ag and TiO_2 nanoparticles on the ultra-thin graphene network. This result provides a potential pathway of incorporation between noble metal and transition metal oxide anchored on carbon-based material to enhance the electrochemical performance of LIBs.

Conflicts of interest

There are no conflicts to declare.

Acknowledgements

Dr. Luo acknowledges the support from USDA National Institute of Food and Agriculture, HSI Collaboration: Integrating Food Science/Engineering and Education Network (IFSEEN, award number: 2015-38422-24059).

Electronic Supplementary Information

Electronic Supplementary Information (ESI) available. See DOI: 10.1039/x0xx00000x.

References

1. H. B. Wu, G. Zhang, L. Yu and X. W. Lou, *Nanoscale Horizons*, 2016, **1**, 27-40.
2. V. Etacheri, R. Marom, R. Elazari, G. Salitra and D. Aurbach, *Energy Environ. Sci.* 2011, **4**, 3243-3262.
3. M. Zheng, H. Tang, L. Li, Q. Hu, L. Zhang, H. Xue and H. Pang, *Adv. Sci.* 2018, **5**, 1700592.

4. G. Tan, F. Wu, Y. Yuan, R. Chen, T. Zhao, Y. Yao, J. Qian, J. Liu, Y. Ye and R. Shahbazian-Yassar, *Nature Commun.* 2016, **7**, 11774.

5. Y. Zhao, X. Li, B. Yan, D. Xiong, D. Li, S. Lawes and X. Sun, *Adv. Energy Mater.* 2016, **6**, 1502175.

6. H. Tabassum, R. Zou, A. Mahmood, Z. Liang, Q. Wang, H. Zhang, S. Gao, C. Qu, W. Guo and S. Guo, *Adv. Mater.* 2018, **30**, 1705441.

7. Y. Wang, S.-Z. Yang, Y. You, Z. Feng, W. Zhu, V. Gariépy, J. Xia, B. Commarieu, A. Darwiche and A. Guerfi, *ACS Appl. Mater. Interfaces*, 2018, **10**, 7061-7068.

8. Z. Zheng, Y. Zao, Q. Zhang, Y. Cheng, H. Chen, K. Zhang, M.-S. Wang and D.-L. Peng, *Chem. Engineer. J.* 2018, **347**, 563-573.

9. Y. Li, Y. Huang, C. Ou, J. Zhu, X. Yuan, L. Yan, W. Li and H. Zhang, *Electrochim. Acta*, 2018, **259**, 474-484.

10. Y. Tang, Y. Zhang, J. Deng, J. Wei, H. L. Tam, B. K. Chandran, Z. Dong, Z. Chen and X. Chen, *Adv. Mater.* 2014, **26**, 6111-6118.

11. D.-H. Lee, B.-H. Lee, A. K. Sinha, J.-H. Park, M.-S. Kim, J. Park, H. Shin, K.-S. Lee, Y.-E. Sung and T. Hyeon, *J. Am. Chem. Soc.* 2018, **140**, 16676-16684.

12. M. Luo, X. Yu, W. Zhao, R. Xu, Y. Liu and H. Shen, *ACS Appl. Mater. Interfaces*, 2018, **10**, 35060-35068.

13. G. Chen, L. Yan, H. Luo and S. Guo, *Adv. Mater.* 2016, **28**, 7580-7602.

14. H. Liu, K. Cao, X. Xu, L. Jiao, Y. Wang and H. Yuan, *ACS Appl. Mater. Interfaces*, 2015, **7**, 11239-11245.

15. Y. Xing, S. Wang, B. Fang, G. Song, D. P. Wilkinson and S. Zhang, *J. Power Sources*, 2018, **385**, 10-17.

16. M. Ren, H. Xu, F. Li, W. Liu, C. Gao, L. Su, G. Li and J. Hei, *J. Power Sources*, 2017, **353**, 237-244.

17. X. Li, B. Zhou, W. Wang, Z. Xu, N. Li, L. Kuang, C. Li, W. Mai, H. Fu and H. Lv, *J. Alloys Compd.* 2017, **706**, 103-109.

18. H. Wang, G. Jia, Y. Guo, Y. Zhang, H. Geng, J. Xu, W. Mai, Q. Yan and H. J. Fan, *Adv. Mater. Interfaces*, 2016, **3**, 1600375.

19. H.-K. Kim, D. Mhamane, M.-S. Kim, H.-K. Roh, V. Aravindan, S. Madhavi, K. C. Roh and K.-B. Kim, *J. Power Sources*, 2016, **327**, 171-177.

20. W. Li, F. Wang, S. Feng, J. Wang, Z. Sun, B. Li, Y. Li, J. Yang, A. A. Elzatahry and Y. Xia, *J. Am. Chem. Soc.* 2013, **135**, 18300-18303.

21. M. Madian, L. Giebeler, M. Klose, T. Jaumann, M. Uhlemann, A. Gebert, S. Oswald, N. Ismail, A. Eychmuller and J. Eckert, *ACS Sustainable Chem. Engineer.* 2015, **3**, 909-919.

22. C. Wang, L. Wu, H. Wang, W. Zuo, Y. Li and J. Liu, *Adv. Funct. Mater.* 2015, **25**, 3524-3533.

23. Y. Luo, J. Li and J. Huang, *Langmuir*, 2016, **32**, 12338-12343.

24. W. S. Hummers Jr and R. E. Offeman, *J. Am. Chem. Soc.* 1958, **80**, 1339-1339.

25. L. Yan, G. Chen, S. Sarker, S. Richins, H. Wang, W. Xu, X. Rui and H. Luo, *ACS Appl. Mater. Interfaces*, 2016, **8**, 22213-22219.

26. L. Yan, J. Yu and H. Luo, *Appl. Mater. Today*, 2017, **8**, 31-34.

27. Z. Zhu, Z. Lu, D. Wang, X. Tang, Y. Yan, W. Shi, Y. Wang, N. Gao, X. Yao and H. Dong, *Appl. Catal. B: Environmental*, 2016, **182**, 115-122.

28. D. Yoon, J. Hwang, D. H. Kim, W. Chang, K. Y. Chung and J. Kim, *J. Supercritical Fluids*, 2017, **125**, 66-78.

29. R. Rajagopal and K.-S. Ryu, *Appl. Catal. B: Environmental*, 2018, **236**, 125-139.

30. M. Thommes, K. Kaneko, A. V. Neimark, J. P. Olivier, F. Rodriguez-Reinoso, J. Rouquerol and K. S. Sing, *Pure Appl. Chem.* 2015, **87**, 1051-1069.

31. C. Li, M. Zhao, C. Sun, B. Jin, C. Yang and Q. Jiang, *J. Power Sources*, 2018, **397**, 162-169.

32. J. Yu, G. Wang, B. Cheng and M. Zhou, *Appl. Catal. B: Environmental*, 2007, **69**, 171-180.

33. J. S. Chen and X. W. Lou, *J. Power Sources*, 2010, **195**, 2905-2908.

34. Z. Chen, Y. Yuan, H. Zhou, X. Wang, Z. Gan, F. Wang and Y. Lu, *Adv. Mater.* 2014, **26**, 339-345.

35. R. van de Krol, A. Goossens and J. Schoonman, *J. Phys. Chem. B*, 1999, **103**, 7151-7159.

36. Z. Jian, B. Zhao, P. Liu, F. Li, M. Zheng, M. Chen, Y. Shi and H. Zhou, *Chem. Commun.* 2014, **50**, 1215-1217.

37. H. Cao, B. Li, J. Zhang, F. Lian, X. Kong and M. Qu, *J. Mater. Chem.* 2012, **22**, 9759-9766.

38. Y. Liu, J. Liu, D. Bin, M. Hou, A. G. Tamirat, Y. Wang and Y. Xia, *ACS Appl. Mater. Interfaces*, 2018, **10**, 14818-14826.

39. L. Shen, E. Uchaker, X. Zhang and G. Cao, *Adv. Mater.* 2012, **24**, 6502-6506.

40. Z.-S. Wu, W. Ren, L. Xu, F. Li and H.-M. Cheng, *ACS nano*, 2011, **5**, 5463-5471.

41. N. Li, G. Zhou, R. Fang, F. Li and H.-M. Cheng, *Nanoscale*, 2013, **5**, 7780-7784.

42. R. Mo, Z. Lei, K. Sun and D. Rooney, *Adv. Mater.* 2014, **26**, 2084-2088.

43. S. Chu, Y. Zhong, R. Cai, Z. Zhang, S. Wei and Z. Shao, *Small*, 2016, **12**, 6724-6734.

44. S. Mehraeen, A. Taşdemir, S. A. Gürsel and A. Yürüm, *Nanotechnol.* 2018, **29**, 255402.

45. R. Meng, H. Hou, X. Liu, W. Hu, J. Duan and S. Liu, *Ceram. Int.* 2015, **41**, 9988-9994.

46. T. Yuan, B. Zhao, R. Cai, Y. Zhou and Z. Shao, *J. Mater. Chem.* 2011, **21**, 15041-15048.

47. W. Zhang, Y. Liu, W. Li, W. Liang and F. Yang, *Appl. Surface Sci.* 2019, **476**, 948-958.